PAPER

Check for updates

First-principles study of ZnO/MoSeTe van der Waals heterostructures for photovoltaic and hydrogen evolution applications

Derese S. Abraham,[ab] Kingsley O. Obodo,*[cde] Aman S. Kassaye, [fg]
Houssam E. Hailouf [h] and Georgies A. Asres [*i]

2D heterostructures possess unique characteristics with potential applications in photocatalytic and photovoltaic devices. In this study, the electronic characteristics of ZnO, Janus MoSeTe monolayers, and heterostructures were investigated using density functional theory calculations. The 2D ZnO and Janus MoSeTe compounds were used to create the ABI-Se, ABI-Te, and ABII-Te stacking configurations. The evaluated 2D ZnO/MoSeTe heterostructures have an indirect band gap semiconductor with an electronic band gap of 1.355 eV, which is suitable for photovoltaic applications. The calculated lattice mismatch for the ZnO/MoSeTe heterostructure is 3.72%, which falls within the acceptable range for experimental realization of van der Waals (vdW) heterostructures. The evaluated power conversion efficiencies (PCE) of the three ZnO/MoSeTe heterostructures are 22.26%, 22.31%, and 22.17% for the ABI-Se, ABI-Te, and ABII-Te stacking configurations, respectively. These heterostructures meet some criteria for water splitting; however, they do not straddle both the conduction band minimum (CBM) and valence band maximum (VBM). The heterostructures satisfy the criteria as potential effective catalysts for the hydrogen evolution reaction (HER). Thus, the 2D ZnO/MoSeTe heterostructures with a high PCE of 22.31%, type-II band alignment, and HER potentials are viable candidate materials for photovoltaic and photocatalytic applications.

1 Introduction

Energy production from renewable resources is critical as the world's future energy demand increasingly depends on them. These resources are either inexhaustible, or regenerate faster than they are consumed. Utilizing a variety of renewable energy sources, such as hydro, solar, and wind, is essential to meet the ever-growing global energy demand.[1,2] The development of

[a]Centre for Materials Engineering, Addis Ababa Institute of Technology, Addis Ababa University, School of Multi-disciplinary Engineering, Addis Ababa, 1000, Ethiopia

[b]Mineral Industry Development Institute, Ministry of Mines, P.O. Box 486, Addis Ababa, Ethiopia

[c]School of Agriculture & Science, University of KwaZulu-Natal, Pietermaritzburg Campus, Private Bag X01, Scottsville, 3209, South Africa. E-mail: obodok@ukzn.ac.za

[d]Center for Space Research, North-West University, Potchefstroom, 2531, South Africa

[e]National Institute of Theoretical and Computational Sciences, Johannesburg, 2000, South Africa

[f]Department of Chemical Engineering, College of Engineering, Addis Ababa Science and Technology University, P.O. Box 16417, Addis Ababa, Ethiopia

[g]Sustainable Energy Center of Excellence, Addis Ababa Science and Technology University, P.O. Box 16417, Addis Ababa, Ethiopia

[h]Materials Science and Informatics Laboratory, Faculty of Science, University of Djelfa, Djelfa, 17000, Algeria

[i]Center for Materials Science and Engineering, College of Natural and Computational Sciences, Addis Ababa University, P. O. Box 1176, Addis Ababa, Ethiopia. E-mail: georgies.alene@aau.edu.et

novel materials for energy conversion,[3] including two-dimensional materials and heterostructures, is gaining significant attention.[4–7] The unique properties of 2D structures, including surface charge, shape, adaptability, and asymmetry, expand their potential applications.[8–10] Janus TMDs, a recent addition to the 2D material family, offer additional advantages such as intrinsic out-of-plane polarization, asymmetric crystal structure, and piezoelectricity.[11–13] WSeTe and MoSeTe monolayers, members of the Janus TMDs, exhibit outstanding absorption in the visible, infrared, and ultraviolet ranges, as shown by both experimental and theoretical studies.[14] A recent study has experimentally demonstrated the synthesis of 2D Janus WSSe and MoSSe monolayers using a modified chemical vapor (CVD) deposition technique.[14,15] These materials have a unique feature due to their broken mirror symmetry, with different atomic species on the top and bottom layers.

Extensive research has been conducted on ZnO nanoparticles because of their remarkable properties, including high photostability, broad radiation absorption,[16] a direct band gap,[17] environmental friendliness, and chemical stability[18] which makes it an attractive option for use in energy conversion such as water-splittng applications and solar cells.[11] Researchers have shown that ZnO can be employed in photovoltaic systems and water-splitting applications due to its high electron mobility, wide band gap, and exceptional stability.

Various strategies have been developed to optimize the performance of 2D materials, including defect engineering, doping, external electric fields, heterojunction design, and heterostructure formation.[7,13,19–22]

Heterostructures based on two-dimensional materials are actively evaluated because they can enhance the properties of the individual monolayers with various potential practical applications.[23] Heterostructures formed between Janus and other 2D van der Waals (vdW) materials can exhibit several fascinating effects.[24] The heterostructures from the combination of Janus MoSSe and WSSe have been shown to have exceptional electronic and optical properties with tuneable properties based on the number of layers and the stacking sequence of the constituent materials.[25] Thus, the combination of 2D ZnO and Janus TMDs can hold significant promise. Previous studies have shown that ZnO–Janus heterostructures are promising for energy-related applications such as solar cells and catalysis.[11]

The present study employs density functional theory (DFT) to investigate the structural stability and electronic characteristics of ZnO/Janus MoSeTe two-dimensional heterostructures with distinct stacking configurations. The interlayer binding energies and electronic band alignments were analyzed to determine the most energetically favorable configuration and to elucidate interfacial interactions. A total of eight possible stacking configurations of the ZnO/MoSeTe heterostructure were initially constructed, considering different atomic registries and surface terminations (Se- or Te-facing). The binding energies of all configurations were calculated to evaluate their thermodynamic stability. The three stacking configurations (ABI-Se, ABI-Te, and ABII-Te) exhibiting the lowest binding energies were identified as the most stable and were therefore selected for detailed electronic, photovoltaic, and photocatalytic analyses.

2 Computational methods

The density functional theory (DFT) method, as implemented in the Quantum ESPRESSO package, was employed in this study. The projector augmented wave (PAW) method was used to compute the monolayers of ZnO, MoSeTe, and the ZnO/MoSeTe Janus heterostructure.[12,13,26] The generalized gradient approximation (GGA) of Perdew, Burke, and Ernzerhof (PBE), with van der Waals (vdW) correction using the Grimme-D2 approach,[12] was applied. The Brillouin zone was sampled using the Monkhorst–Pack scheme with a $20 \times 20 \times 1$ k-point grid. The geometric structures were relaxed until all atomic forces were below 1 meV Å^{-1}.

The plane-wave cutoff energy was set to 70 Ry, and a vacuum thickness of 20 Å was applied perpendicular to the surface[27] Since the PBE approximation is known to underestimate band gap values for monolayers and heterostructures. Thus, the Heyd–Scuseria–Ernzerhof (HSE) exchange correlation functional as implemented in Quantum ESPRESSO package was also used to evaluate the electronic structure.

The binding energy of the heterostructures was computed using the equation described below (eqn (1)).[28]

$$E_b = E_{\text{MoSeTe/ZnO}} - (E_{\text{MoSeTe}} + E_{\text{ZnO}}) \qquad (1)$$

where, E_b represents the binding energy. E_{ZnO}, E_{MoSeTe}, and $E_{\text{MoSeTe/ZnO}}$ are the total energies of ZnO, Janus MoSeTe, and the heterostructure, respectively.

3 Result and discussion

3.1 Structural properties for monolayer and heterostructure

The computed lattice constants are 3.27 Å and 3.40 Å for ZnO and MoSeTe monolayers, respectively. These structural parameters are consistent with previous findings.[29–31]

Zinc oxide (ZnO) crystallizes in the wurtzite structure and belongs to the $P6_3mc$ space group, characteristic of the hexagonal crystal system. This structure exhibits high symmetry, with zinc and oxygen atoms arranged in tetrahedral coordination. The hexagonal symmetry plays a crucial role in determining the material's electronic and optical properties, making ZnO suitable for a wide range of technological applications. Molybdenum selenide telluride (MoSeTe) adopts a layered crystal structure with the $P\bar{3}m1$ space group, belonging to the trigonal crystal system. In this arrangement, molybdenum, selenium, and tellurium atoms form distinct layers held together by van der Waals forces. The trigonal symmetry contributes to the material's unique electronic characteristics, making it a promising candidate for advanced materials applications. After analyzing the properties of the individual monolayers, eight different stacking configurations of the ZnO/MoSeTe heterostructure were constructed, and their binding energies (E_b) were calculated to evaluate their thermodynamic stability.[12,13,32] For detailed analysis, we selected three representative heterostructures: ABI-Te, ABI-Se, and ABII-Te. In these labels, "AB" indicates the stacking arrangement in which the two hexagonal lattices are placed on top of each other. The Roman numerals I and II denote whether the Zn atom is positioned beneath the Mo atom or beneath the Se/Te atom of the Janus MoSeTe monolayer. The suffixes "Te" and "Se" specify that the tellurium or selenium atoms of the Janus layer are facing the ZnO monolayer. These three configurations were chosen to explore how stacking sequence and surface termination influence the structural stability and electronic properties of the ZnO/MoSeTe heterostructures. The heterostructures that exhibit the lowest (most
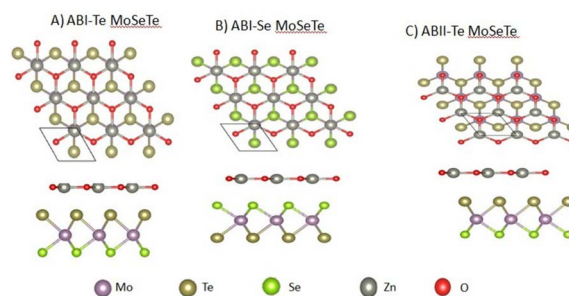

Fig. 1 Stacking patterns of the three most stable ZnO/MoSeTe heterostructures: (A) ABI-Te MoSeTe, (B) ABI-Se MoSeTe, and (C) ABII-Te MoSeTe.

Table 1 Lattice parameters and lattice mismatches of monolayers calculated using PBE

MXY	Reference a (Å)	Calculated a (Å)	Mismatch (%)
ZnO	3.29 (ref. 36)	3.27	—
MoSeTe	3.42 (ref. 9)	3.40	3.72

Fig. 3 The PDOS of (a) MoSeTe Monolayers and (b) ZnO.

negative) binding energy and the most stable stacking modes of the ZnO/MoSeTe heterostructures (see Fig. 1) are selected for further investigation. The lattice mismatch of ZnO/MoSeTe is calculated to be 3.72%, which is acceptable and indicates that the fabrication of these vdW heterostructures is experimentally feasible, as it falls below the commonly accepted 5% lattice mismatch threshold.[33,34] Table 1 demonstrates that the lattice mismatch between the calculated lattice parameters of the two monolayers is less than 5%, and the ZnO and MoSeTe layers are perfectly coherent.

The lattice mismatch calculation was performed using the formula.[35] The reference lattice parameters are taken from.[9,36]

$$\text{Lattice mismatch}(\%) = \frac{a_{\text{JTMDs}} - a_{\text{ZnO}}}{a_{\text{JTMDs}}} \times 100\% \qquad (2)$$

3.2 Electronic properties of MoSeTe and ZnO

Janus MoSeTe and ZnO monolayers are found to be semiconductors with band gaps of 1.49 eV and 1.68 eV, respectively, as calculated using the PBE functional. To obtain more accurate band gap values, the Heyd–Scuseria–Ernzerhof (HSE) hybrid functional was also employed. Consequently, the HSE06 functional was employed in addition to PBE for our calculations, and the band gap values for MoSeTe and ZnO were 1.86 eV and 2.99 eV, respectively. The band gap values calculated by HSE06 are larger than those calculated by PBE. The larger band gap values obtained with the HSE06 functional arise from the well-known tendency of PBE to underestimate band gaps. These results are in good agreement with previous studies.[9,11,31] Fig. 2(a) and (b), as well as Fig. 3(a) and (b), present the

electronic band structures and partial density of states (PDOS) for the MoSeTe and ZnO monolayers, respectively.

Fig. 2 shows the electronic band structures of the ZnO and MoSeTe monolayers calculated using both PBE and HSE06 functionals. At the PBE level, ZnO exhibits a direct bandgap, with both the valence band maximum (VBM) and conduction band minimum (CBM) located at the Γ point, consistent with previous reports for monolayer ZnO. The HSE06 calculations preserve this direct-gap nature while yielding a wider bandgap, reflecting the well-known bandgap underestimation of PBE. In contrast, MoSeTe displays an indirect bandgap, with the VBM located at the K point and the CBM positioned between the Γ and K points. This bandgap character remains unchanged upon inclusion of the HSE06 functional, although the bandgap magnitude increases, confirming that HSE06 mainly provides a quantitative correction without altering the qualitative electronic features of the monolayers. As shown in Fig. 3, the Mo-4d orbitals dominate the states near the Fermi level for both the VBM and CBM in MoSeTe, while the O-2p orbitals mainly contribute to the VBM of ZnO. The conduction band of MoSeTe primarily consists of Mo-4d and Se-2p states, with Mo-4d being the most significant in the 0.5–3.8 eV range. Additionally, the O-2p states are prevalent in ZnO at energies well below the CBM. Table 2 shows the calculated values for the monolayers' lattice constants, band gaps, work functions, and valence and conduction band edges.

3.2.1 Electronic properties of MoSeTe/ZnO heterostructure. The influence of different stacking arrangements on the electronic structure and band gap of the ZnO/MoSeTe heterostructures was investigated. Table 3 presents the calculated optimized lattice constant a (Å), band gap values (PBE and HSE, in eV), work function (in eV), and the valence and conduction band edge positions relative to the vacuum level (E_{VB} and E_{CB}).
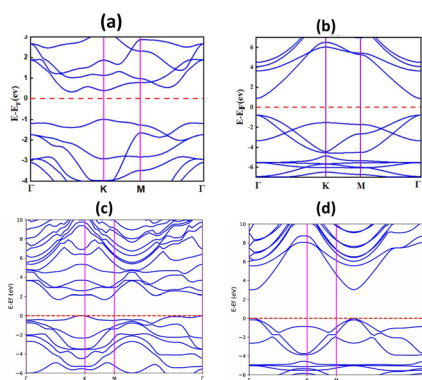

Fig. 2 Electronic band structures of the isolated monolayers: (a) MoSeTe calculated using the PBE functional, (b) ZnO calculated using the PBE functional, (c) MoSeTe calculated using the HSE06 functional, and (d) ZnO calculated using the HSE06 functional.
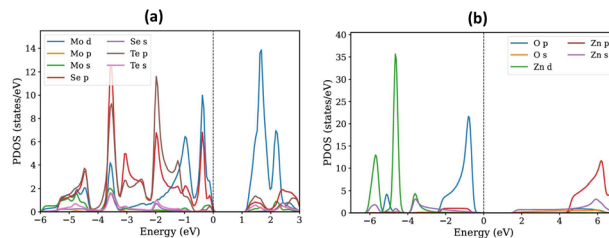
Table 2 Calculated structural and electronic parameters of the monolayers, including the lattice constant, band gap, work function, and the valence and conduction band edge positions

Monolayer	ZnO	MoSeTe
a (Å)	3.27	3.40
E_{g} (PBE)	1.676	1.487
E_{g} (HSE06)	2.986	1.856
φ (eV)	5.064	5.074
E_{VBM} (eV)	−5.062	−5.070
E_{CBM} (eV)	−3.385	−3.583

Table 3 Optimized lattice constant a (Å), calculated band gap (PBE and HSE, in eV), work function (eV), and the valence and conduction band edge positions with respect to the vacuum level (E_{VB} and E_{CB}) for the heterostructure

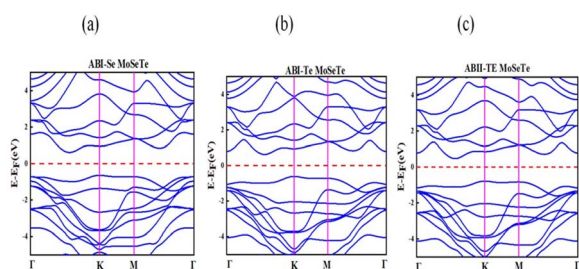| Heterostructure	ABI-Se MoSeTe	ABI-Te MoSeTe	ABII-Te MoSeTe
a (Å)	3.3269	3.3269	3.3269
E_g (PBE)	1.385	1.318	1.39
E_g (HSE06)	1.349	1.327	1.355
φ (eV)	4.982	5.061	5.049
E_{VBM} (eV)	−4.99	−4.99	−5
E_{CBM} (eV)	−3.605	−3.672	−3.61

Fig. 4 Electronic band structures of the ZnO/MoSeTe heterostructures: (a) ABI-Se, (b) ABI-Te, and (c) ABII-Te stacking configurations.

The valence band maximum (VBM) of the three ZnO/MoSeTe heterostructure stacking patterns is located along the K path in the Brillouin zone, while the conduction band minimum (CBM) is slightly shifted to the left of the K path, as illustrated in Fig. 4(a–c). This indicates that all three configurations exhibit an indirect band gap, inheriting the indirect nature of the MoSeTe monolayer.

The orbital-projected density of states (PDOS) was analyzed to investigate the electronic contributions of individual atoms within each heterostructure. As illustrated in Fig. 5(A–C), the states near the Fermi level in the ZnO/MoSeTe heterostructures are mainly derived from Mo-4d, Se-4p, Te-5p, and O-2p orbitals, corresponding to the Mo, Se, Te, and O atoms, respectively. The conduction band minimum (CBM) and valence band maximum (VBM) near the Fermi level are dominated by the Mo-4d orbital. The upper valence band of the ZnO/MoSeTe heterostructure is primarily composed of Zn-3d and O-2p orbitals, with a significant contribution from Zn-3d states. Conversely, the lower conduction band is mainly composed of Mo-4d and Te-2p
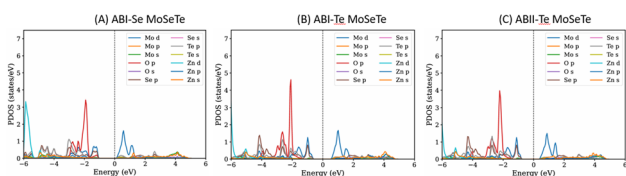
states, with Mo-4d being the dominant contributor. From this analysis, we observe that the valence band (VB) edges are primarily contributed by ZnO, whereas the conduction band (CB) edges are dominated by MoSeTe. Our orbital-projected density of states (PDOS) discussed below shows this is true for ABI-Se MoSeTe. This type-II band alignment is advantageous for applications requiring efficient separation of electrons and holes. Such exciton separation is crucial for enhancing the performance of photovoltaic devices and photocatalytic water-splitting systems. Therefore, these ZnO/MoSeTe heterostructures demonstrate strong potential for next-generation energy conversion applications. In the following section, their photocatalytic and photovoltaic performance is evaluated to further assess their suitability for solar-driven energy technologies.

3.2.2 ZnO/MoSeTe heterostructures for photocatalysis. The band edge values, as well as band gap width, are critical characteristics in semiconductor photocatalyst materials. The band edge values of the photocatalyst materials must compared with the reduction and oxidation potentials of water at a specific pH level in order determine if the material is suitable for water splitting.[23] For the simultaneous occurrence of hydrogen and oxygen evolution reactions in photocatalytic water splitting, the band edges must span the reduction and oxidation potentials of water at a specific pH value. During the formation of hydrogen and oxygen, the energy at the lowest point of the conduction band (CBM) must exceed the energy required to reduce water into H^+/H_2 (reduction potential, −4.44 eV). Conversely, the energy at the highest point of the valence band (VBM) must be lower than the energy required for the oxidation of H_2O to O_2 (oxidation potential, −5.67 eV).[23,37]

Fig. 6 depicts the band edge positions of the ABI-Se, ABI-Te, and ABII-Te MoSeTe heterostructures. As shown in panel (b), the energetically stable ZnO/MoSeTe stacking exhibits a type-II band alignment, which promotes efficient charge-carrier separation and enhances the photocatalytic activity for water splitting. The suitability of these 2D heterostructures as potential catalysts for the hydrogen evolution reaction (HER) is evaluated by comparing their band edge positions with the redox potentials of water.[38,39] The conduction band minima (CBM) of the ABI-Se MoSeTe, ABI-Te MoSeTe, and ABII-Te MoSeTe

Fig. 5 The PDOS of the ZnO/MoSeTe heterostructure stacking patterns is presented for: (A) ABI-Se MoSeTe, (B) ABI-Te MoSeTe, and (C) ABII-Te MoSeTe.
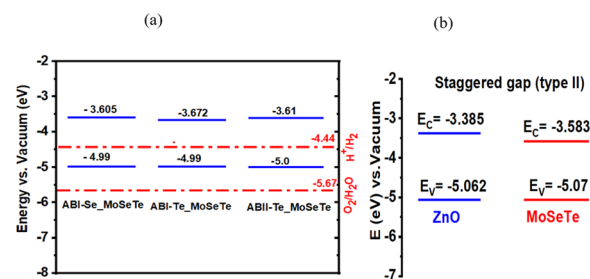

Fig. 6 (a) Band edge positions of the three ZnO/MoSeTe heterostructures relative to the redox potentials of water. (b) Schematic illustration of the type-II band alignment in the ABII-Te MoSeTe heterostructure.
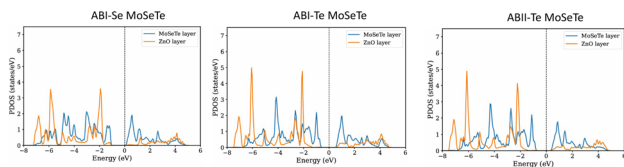
Fig. 7 Layred resolved projected density of state of the three heterostructures.

heterostructures lie above the H^+/H_2 reduction potential, confirming their capability to drive the hydrogen evolution reaction (HER).

To further investigate the electronic contributions of the individual layers and verify the band alignment, the layer-resolved (projected) density of state was analyzed for the most stable stacking configurations (Fig. 7). Our analysis confirms that. For the case of ABI-Se MoSeTe the valence band maximum edge is contributed by ZnO layer (even if the MoSeTe contribution is in the proximity) and the CBM by MoSeTe layer confirming that it is type II band gap alignment. But for the other heterostructures it is type I band gap alignment. In another study we have shown that strain can be used as a knob to tune the band edge alignments,[36] we suggest that to enhance the performance of this structure for efficient charge carrier separation and improve for photocatalytic and photovoltaic applications to do the same strain engineering.

3.2.3 PCE of ZnO/MoSeTe heterostructures for photovoltaic. The three most stable heterostructure configurations exhibit type-II band alignment, which is essential for efficient photovoltaic energy conversion. Their photovoltaic conversion efficiency (PCE) was estimated using the open-circuit voltage (V_{OC}), short-circuit current (I_{SC}), and fill factor (FF), which are key parameters for characterizing the performance of a photovoltaic device.[40]

The power conversion efficiency of the considered heterostructures were evaluated using eqn (2).

$$\text{PCE} = \frac{\text{FF } V_{OC} J_{SC}}{P_{sun}} \tag{3}$$

$$eV_{OC} = E_g - E_{loss} \tag{4}$$

$$P_{sun} = \int_0^\infty S(E) \mathrm{d}E \tag{5}$$

$$J_{SC} = \int_{E_g}^\infty \frac{S(E)}{E} \mathrm{d}E \tag{6}$$

where $S(E)$ is the solar power supplied per unit area and photon energy, V_{OC} is the open-circuit voltage, J_{SC} is the short-circuit current, E is the photon energy, and FF is the fill factor. A previous experimental study determined the fill factor of the MoS$_2$/p-Si heterostructure to be 0.57.[41] This fill factor was applied in the current study for the considered transition metal dichalcogenide system. The value of $S(E)$ is calculated using the NREL AM1.5 dataset. For the energy loss in 2D materials, we examine values of 0.2 and 0.3.[40,42] The theoretically computed

power conversion efficiency (PCE) values for the ABI-Se MoSeTe, ABII-Te MoSeTe, and ABI-Te MoSeTe heterostructures are 22.26%, 22.17%, and 22.31%, respectively. These values are significantly higher than that reported for the WSe$_2$/MoS$_2$ heterostructure (2.56%)[43] and the MoS$_2$/p-Si heterostructure (5.23%).[42] The current study demonstrates enhanced power conversion efficiency and confirms the presence of type-II band alignment in the investigated heterostructures, making these systems promising candidates for future solar cell applications compared to other study in the area.[44–47]

The calculated high PCE values (averaging ~22.2%) highlight the efficient light-harvesting and photovoltaic potential of the ZnO/MoSeTe heterostructures. This performance, complemented by the band edge alignments shown in Fig. 6, confirms their suitability for dual energy applications, specifically high-efficiency solar cells and photocatalytic hydrogen evolution.

4 Conclusions

First-principles DFT calculations were performed to investigate the structural and electronic properties of MoSeTe/ZnO van der Waals heterostructures as potential candidates for photovoltaic devices and photocatalytic water-splitting applications. Based on binding energy calculations, the most stable heterostructure stacking configurations were identified as ABI-Se, ABI-Te, and ABII-Te, selected from eight different stacking arrangements. All three heterostructures exhibit an indirect bandgap with ABI-Se exhibiting type-II band alignment. The highest band gap was found to be 1.39 eV for the ABII-Te MoSeTe/ZnO stacking configuration. Although these heterostructure configurations do not fully meet the band edge criteria for overall water splitting, they exhibit favorable photocatalytic activity for the hydrogen evolution reaction (HER). The ABI-Se, ABI-Te, and ABII-Te stacking configurations of MoSeTe/ZnO show power conversion efficiencies exceeding 22%, highlighting their significant potential for photovoltaic applications. Furthermore, tuning the band edges through strain or doping offers a promising route to enhance the photocatalytic performance, potentially making these heterostructures suitable for complete water-splitting applications.

Detailed optical absorption analysis of the ZnO/MoSeTe heterostructures, including comparison with the constituent monolayers, will be an important subject of future work once adequate computational resources are available. We believe this clarification improves the transparency of the study while maintaining its scientific validity. We also clarify that the evaluation of HER activity is based on band-edge alignment relative to the $H^+/H2$ reduction potential, which provides a necessary thermodynamic criterion for HER feasibility but does not account for reaction kinetics. This is a limitation in our study and a comprehensive analysis of the hydrogen adsorption free energy (ΔG_{H*}) at relevant active sites is identified as an important direction for future work.

Conflicts of interest

There are no conflicts to declare.

Data availability

The data supporting the findings of this study are available within the article. The computational data supporting the findings of this study, including the DFT input files, output files, structural models, and analysis scripts, are available from the corresponding author upon reasonable request.

Acknowledgements

Notes and references

1 A. Holt and I. J. Pengelly, *IET Road Transport Information and Control Conference and the ITS United Kingdom Members' Conference (RTIC 2008)*, 2008, p. 55.

2 N. L. Panwar, S. C. Kaushik and S. Kothari, *Renewable Sustainable Energy Rev.*, 2011, **15**, 1513–1524.

3 A. K. Sibhatu, G. A. Asres, A. Yimam and T. Teshome, *RSC Adv.*, 2022, **12**, 21270–21279.

4 I. C. Onyia, S. O. Ezeonu, D. Bessarabov and K. O. Obodo, *Comput. Mater. Sci.*, 2021, **197**, 110613.

5 K. Obodo, G. Gebreyesus, C. Ouma, J. Obodo, S. Ezeonu, D. Rai and B. Bouhafs, *RSC Adv.*, 2020, **10**, 15670–15676.

6 K. O. Obodo, C. N. M. Ouma, J. T. Obodo, M. Braun and D. Bessarabov, *Comput. Condens. Matter*, 2019, **21**, e00419.

7 K. O. Obodo, C. N. M. Ouma, J. T. Obodo and M. Braun, *Phys. Chem. Chem. Phys.*, 2017, **19**, 19050–19057.

8 Y. Khan, S. M. Obaidulla, M. R. Habib, A. Gayen, T. Liang, X. Wang and M. Xu, *Nano Today*, 2020, **34**, 100902.

9 S. Saini, A. Shrivastava, A. Dixit and S. Singh, *J. Mater. Sci.*, 2022, **57**, 7012–7022.

10 B. Peng, P. K. Ang and K. P. Loh, *Nano Today*, 2015, **10**, 128–137.

11 M. Idrees, H. Din, S. U. Rehman, M. Shafiq, Y. Saeed, H. Bui, C. V. Nguyen and B. Amin, *Phys. Chem. Chem. Phys.*, 2020, **22**, 10351–10359.

12 X. Li, L. Wu, S. Cheng, C. Chen and P. Lu, *RSC Adv.*, 2022, **12**, 2292–2299.

13 S. T. Ayele, K. O. Obodo and G. A. Asres, *RSC Adv.*, 2022, **12**, 31518–31524.

14 S. Kar, P. Kumari, M. V. Kamalakar and S. Ray, *Sci. Rep.*, 2023, **13**, 13696.

15 L. Ju, X. Tang, J. Li, H. Dong, S. Yang, Y. Gao and W. Liu, *Molecules*, 2023, **28**, 4602.

16 S. Raha and M. Ahmaruzzaman, *Nanoscale Adv.*, 2022, **4**, 1868–1925.

17 M. A. Borysiewicz, *Crystals*, 2019, **9**, 505.

18 A. B. Djurišić and Y. H. Leung, *small*, 2006, **2**, 944–961.

19 K. O. Obodo, C. N. M. Ouma, P. M. Modisha and D. Bessarabov, *Appl. Surf. Sci.*, 2020, **529**, 147186.

20 B. Chettri, P. Patra, T. V. Vu, C. Q. Nguyen, A. Yaya, K. O. Obodo, N. T. T. Tran, A. Laref, D. Rai, *et al.*, *Phys. E*, 2021, **126**, 114436.

21 K. O. Obodo, C. N. Ouma, G. Gebreyesus, J. T. Obodo, S. O. Ezeonu and B. Bouhafs, *Mater. Res. Express*, 2019, **6**, 106307.

22 K. O. Obodo, N. Chetty and J. Obodo, *Comput. Mater. Sci.*, 2017, **128**, 373–378.

23 A. Rawat, M. K. Mohanta, N. Jena, R. Ahammed and A. De Sarkar, *J. Phys. Chem. C*, 2020, **124**, 10385–10397.

24 M. Yagmurcukardes, Y. Qin, S. Ozen, M. Sayyad, F. M. Peeters, S. Tongay and H. Sahin, *Appl. Phys. Rev.*, 2020, **7**, year.

25 D. D. Vo, T. V. Vu, T. H. T. Nguyen, N. N. Hieu, H. V. Phuc, N. T. Binh, M. Idrees, B. Amin and C. V. Nguyen, *RSC Adv.*, 2020, **10**, 9824–9832.

26 A. kassaye Sibhatu, T. Teshome, O. Akin-Ojo, A. Yimam and G. A. Asres, *RSC Adv.*, 2022, **12**, 30838–30845.

27 S. Roy and P. Bermel, *Sol. Energy Mater. Sol. Cell.*, 2018, **174**, 370–379.

28 X. Wang, Y. Wang, R. Quhe, Y. Tang, X. Dai and W. Tang, *J. Alloys Compd.*, 2020, **816**, 152559.

29 V. Jafarova and G. Orudzhev, *Solid State Commun.*, 2021, **325**, 114166.

30 J. Geurts, *Zinc Oxide: from Fundamental Properties towards Novel Applications*, Springer, 2010, pp. 7–37.

31 X. Yang, D. Singh, Z. Xu, Z. Wang and R. Ahuja, *J. Mater. Chem. C*, 2019, **7**, 12312–12320.

32 S. Wang, C. Ren, H. Tian, J. Yu and M. Sun, *Phys. Chem. Chem. Phys.*, 2018, **20**, 13394–13399.

33 P. Solís-Fernández, M. Bissett and H. Ago, *Chem. Soc. Rev.*, 2017, **46**, 4572–4613.

34 J.-C. Blancon, J. Even, C. C. Stoumpos, M. G. Kanatzidis and A. D. Mohite, *Nat. Nanotechnol.*, 2020, **15**, 969–985.

35 X. Li and R. Yang, *Phys. Rev. B Condens. Matter*, 2012, **86**, 054305.

36 E. Peterson, T. Debela, G. Gomoro, J. Neaton and G. Asres, *RSC Adv.*, 2022, **12**, 31303–31316.

37 B. T. Beshir, K. O. Obodo and G. A. Asres, *RSC Adv.*, 2022, **12**, 13749–13755.

38 D. Zheng, L. Yu, W. Liu, X. Dai, X. Niu, W. Fu, W. Shi, F. Wu and X. Cao, *Cell Rep. Phys. Sci.*, 2021, **2**(6), 100443.

39 H. Hu and J.-H. Choi, *RSC Adv.*, 2020, **10**, 38484–38489.

40 M. M. Furchi, F. Höller, L. Dobusch, D. K. Polyushkin, S. Schuler and T. Mueller, *npj 2D Mater. Appl.*, 2018, **2**, 3.

41 S. K. Pradhan, B. Xiao and A. K. Pradhan, *Sol. Energy Mater. Sol. Cells*, 2016, **144**, 117–127.

42 K. Lai, C.-L. Yan, L.-Q. Gao and W.-B. Zhang, *J. Phys. Chem. C*, 2018, **122**, 7656–7663.

43 M.-L. Tsai, M.-Y. Li, J. R. D. Retamal, K.-T. Lam, Y.-C. Lin, K. Suenaga, L.-J. Chen, G. Liang, L.-J. Li and J.-H. He, *Adv. Mater.*, 2017, **29**, 1701168.

44 C. D. Abernethy, G. M. Codd, M. D. Spicer and M. K. Taylor, *J. Am. Chem. Soc.*, 2003, **125**, 1128–1129.

45 F. A. Cotton, G. Wilkinson, C. A. Murillio and M. Bochmann, *Advanced Inorganic Chemistry*, Wiley, Chichester, 6th edn, 1999.

46 A. J. Arduengo, III, H. V. R. Dias, R. L. Harlow and M. Kline, *J. Am. Chem. Soc.*, 1992, **114**, 5530–5534.

47 L. N. Appelhans, D. Zuccaccia, A. Kovacevic, A. R. Chianese, J. R. Miecznikowski, A. Macchioni, E. Clot, O. Eisenstein and R. H. Crabtree, *J. Am. Chem. Soc.*, 2005, **127**, 16299–16311.